

Modelling the Performance of Double Pass Solar Air Collectors


Maytham H. Machi^{1,*}, Istvan Farkas², and Janos Buzas²

ABSTRACT

This study presents a detailed investigation into the thermal performance of double-pass solar air collectors (DPSACs) through a combination of experimental testing and theoretical modelling. DPSACs are widely recognized for their ability to enhance heat transfer and reduce energy losses, making them suitable for applications such as drying and space heating. Experimental measurements were conducted under outdoor conditions focusing on key operational parameters such as mass flow rates (MFR) and solar radiation intensity. A theoretical model was developed and validated against experimental data, achieving high agreement with R^2 values of 0.989 for outlet temperature and 0.917 for thermal efficiency. Results indicate that increasing MFRs initially improves thermal efficiency by enhancing convective heat transfer. However, higher MFRs reduce the outlet air temperature, as shorter air residence times limit the transfer of heat to the air. Solar radiation was found to have a pronounced effect at lower MFRs, emphasizing the need for optimal MFR selection to balance efficiency and temperature output. The study highlights a preferred operating range of 0.01–0.025 kg/s for maintaining efficient thermal performance under varying solar intensities. The validated model provides a robust framework for predicting the performance of DPSACs under diverse conditions.

Submitted: November 26, 2024

Published: January 30, 2025

 10.24018/ejenergy.2025.5.1.159

¹ Doctoral School of Mechanical Engineering, Hungarian University of Agriculture and Life Sciences, Hungary.

² Institute of Technology, Hungarian University of Agriculture and Life Sciences, Hungary.

* Corresponding Author:
e-mail: CFL06K@uni-mate.hu

Keywords: Air heater, Collector efficiency, thermal efficiency, V-ribs.

1. INTRODUCTION

The expansion of solar energy is driven by rising fuel costs and growing environmental awareness. Among solar energy various applications, solar air collectors (SACs) have gained popularity due to their potential for providing effective thermal energy solutions [1], [2]. Due to its low thermal efficiency, SAC is a focus of ongoing research aimed at improving its performance [3].

Several studies have focused on improving design and material selection to enhance the efficiency of SACs. One effective approach involves increasing the number of air passes and separating the flow streams. Research indicates that replacing single-pass configurations with double or multiple-pass systems significantly reduces radiative and convective heat losses to the environment, thereby minimizing overall thermal losses [4]. In addition to modifying the number of air passes, other advancements include optimizing airflow patterns, enhancing duct geometry, increasing the number of glazing covers, improving

absorber plate geometry, and incorporating turbulators and fins to enhance heat transfer [5].

Omotosho *et al.* [6] developed a mathematical model and performed experimental tests on a low-cost SAC using upcycled aluminium cans. They determined that increasing the air passes to ten produced the highest useful energy, outperforming single-pass and five-pass designs in terms of temperature and efficiency.

Karim *et al.* [7] utilized MATLAB to create a computational model for corrugated double-pass air collectors (DPSACs), achieving a maximum deviation of 7% when validated against experimental results. The analysis highlighted solar radiation, mass flow rate (MFR), inlet air temperature, and collector length as critical parameters affecting efficiency. Among these, MFR and inlet temperature emerged as the most influential.

Singh *et al.* [8] analysed the thermal, effective, and exergetic efficiencies of double-pass parallel flow SAC using a MATLAB-based model. The findings showed excellent alignment between the model predictions and



experimental observations, with optimal thermal performance achieved at lower Reynolds numbers and minimal changes beyond 18,000.

Sun *et al.* [9] developed a numerical model for forced convection SACs, validated through indoor experiments. Results indicated a close match between theoretical calculations and experimental outcome. The study concluded that varying the MFR is essential to maximizing SAC performance, as several optimal MFRs were identified for specific solar intensity levels.

Bangura *et al.* [10] studied a DPSAC for drying applications using a steady-state thermal network model. The finding revealed that an MFR of 0.02 kg/s produced an outlet air temperature of 91.72 °C, while thermal efficiency improved significantly from 29% to 67% as the MFRs increased from 0.01 to 0.3 kg/s. Among the tested collector lengths, 1.4 m and 2.4 m were found to be cost-effective, with the model's predictions showing consistency with earlier research findings.

El-Sebaï *et al.* [11] proposed a transient mathematical model for a single-pass SAC, demonstrating that a nickel–tin selectively coated absorber enhanced annual efficiency by 29.23% over a black-painted absorber. The model's predictions exhibited a daily average error of 7.7%.

Lin *et al.* [12] evaluated SACs with corrugated absorbers through experiments and modelling, highlighting surface absorptance and opening angle as key efficiency factors. A 60° angle with 0.8 absorptance achieved 27.14% efficiency, comparable to 120° with 0.96, providing insights for SAC design.

Saravanakumar *et al.* [13] analysed SACs with arc-shaped ribs, fins, and baffles, achieving 28.3% higher thermal efficiency and 27.1% better effective efficiency than conventional designs. Lower baffle width and length maximized performance at higher MFRs. Predictive correlations showed a 13% deviation, and the model was validated against existing studies.

Assadeg *et al.* [14] carried out a theoretical study on a DPSAC integrated with fins and a PCM for energy storage. Their findings revealed that the proposed design achieved a highest energy efficiency of 73% at a MFR of 0.15 kg/s. The exergy efficiency was observed to vary between 2.5% and 4.2% at a solar intensity of 1000 W/m².

A comprehensive review of research on SACs reveals a variety of strategies aimed at improving their thermal performance and efficiency. Increasing the number of air passes, such as transitioning from single- to double- or multi-pass configurations, has been widely studied for its ability to reduce radiative and convective losses while enhancing overall heat retention. The use of fins and turbulators has also emerged as a key method for boosting thermal efficiency by promoting turbulence, improving heat transfer, and optimizing airflow distribution. Advanced absorber designs, such as corrugated or selectively coated surfaces, have been shown to significantly enhance energy absorption and minimize heat losses. Additionally, incorporating phase change materials (PCMs) in SACs has proven effective for thermal energy storage, enabling consistent performance during fluctuating solar conditions. These advancements demonstrate the importance of tailored design and material innovations in

maximizing the efficiency of SACs across diverse applications, including drying and thermal energy systems.

The current study presents a theoretical model validated with experimental results to estimate the performance of DPSACs, providing a reliable framework for optimizing design and operational parameters. These advancements demonstrate the importance of tailored design and material innovations in maximizing the efficiency of SACs across diverse applications, including drying and thermal energy systems.

2. MATERIALS AND METHODS

2.1. Setup Details and Instrumentation

The current investigation comprises both theoretical and experimental components. The experimental investigation was carried out at the Solar Energy Laboratory of the Hungarian University of Agriculture and Life Sciences (MATE) in Gödöllő, Hungary, as shown in Fig. 1. The experiments were conducted under predominantly clear and sunny conditions between August and September 2024.

The experiments were conducted using a DPSAC featuring a copper absorber plate with dimensions of 1.2 m × 0.46 m. The upper channel, with a depth of 5.5 cm, was formed by the absorber plate and a transparent plastic cover. The collector's outer casing was constructed from wood, while the base comprised a layered structure of two 3 mm thick wooden sheets, with a 2 cm layer of extruded polystyrene (XPS) insulation sandwiched between them. The bottom channel, measuring 3.5 cm in depth, was equipped with six buffers to direct airflow efficiently through the channel. Fig. 2 present schematic view of the rig structure. Fig. 3 presents a photograph of the tested rig.

Table I provides a summary of the measurement instruments, including their accuracy and operational ranges. A total of 14 T-type thermocouples were employed to record temperature measurements: four for ambient and inlet conditions, four at the outlet port, and six attached to the absorber plate to monitor its temperature. The MFR was measured using an orifice plate meter paired with a differential pressure (DP) sensor, while solar radiation intensity was logged using a pyranometer. Fig. 4 present a schematic representation of the test setup, along with sensor positions.

2.2. Theoretical Analysis

The thermal analysis of a SAC can be systematically developed by incorporating specific assumptions that simplify the modelling process. These foundational assumptions, adapted from the research [15]–[17], are as follows: (i) The system is assumed to operate under steady-state conditions with heat transfer occurring in one dimension, (ii) heat transfer to the air is considered uniform along the collector's length, (iii) the ambient wind speed is treated as constant during the analysis, (iv) airflow inside the collector is evenly distributed, resulting in a linear variation of air temperature along its length, and (v) edge losses are neglected due to the system's effective insulation.

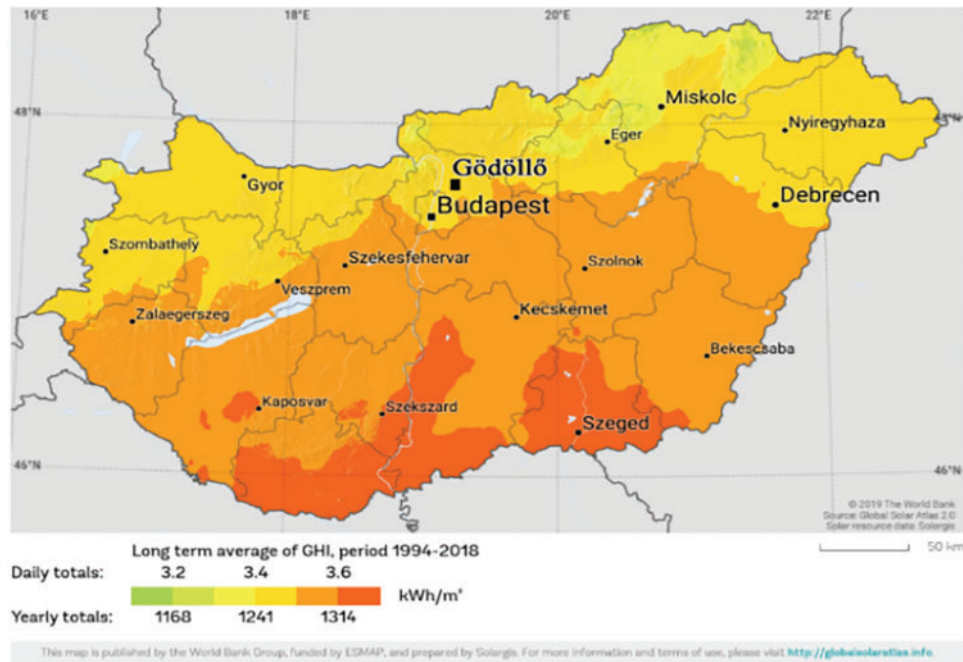


Fig. 1. Geographical location of the study city.

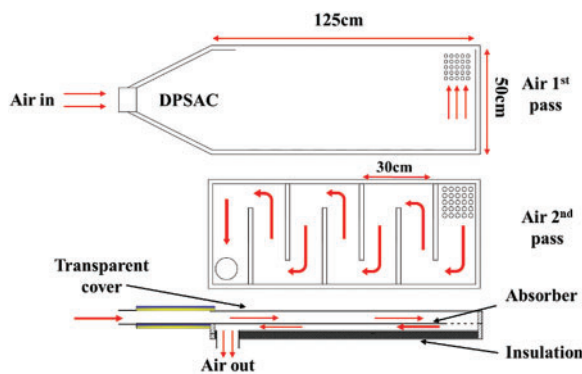


Fig. 2. Schematic of the rig structure.

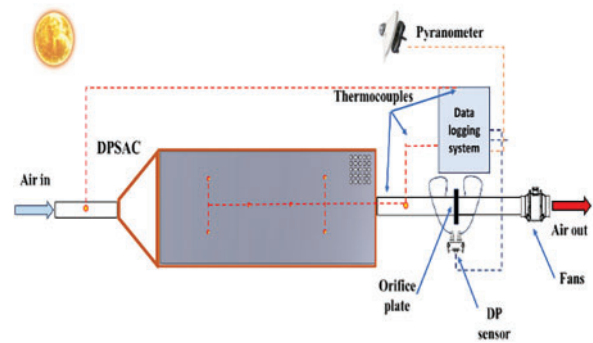


Fig. 4. Schematic view of the experimental setup.

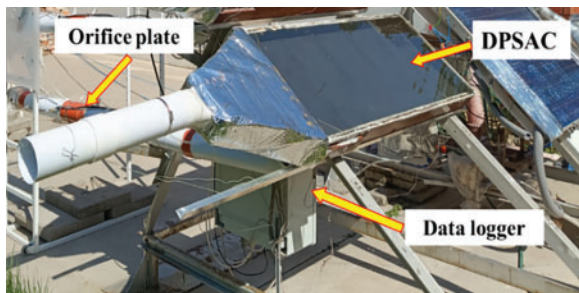


Fig. 3. Photograph of the tested rig.

The heat balance equations represent the energy exchanges occurring at critical locations within the solar

air collector system, as reflected in Fig. 5, which illustrates the heat transfer coefficients and the thermal resistance network corresponding to these points. The following equations describe these energy exchanges:

For the transparent cover at T_1 , the energy balance equation is given as:

$$I \alpha_g + h_{r21} (T_2 - T_1) + h_1 (T_{f1} - T_1) = U_t (T_1 - T_a). \quad (1)$$

For the air in the first channel at T_{f1} , the energy balance is given as:

$$h_2 (T_2 - T_{f1}) = h_1 (T_{f1} - T_1) + Q_{ul}. \quad (2)$$

TABLE I: MEASUREMENT INSTRUMENTS SPECIFICATIONS

Parameter	Device	Range	Accuracy
Temperature	Tx-thermocouple	-250~250 °C	±0.5 °C
Solar radiation	Kipp & Zonen CM11	0~1400 W/m²	±<0.6%, <1000 W/
Orifice pressure drop (MFR)	SENSIRION, SDP-816 DP sensor	-500~500 pa	±3%
Data logging system	ADAM (4018+, 4017)	-100~400 °C, 0~10 V	±0.1%

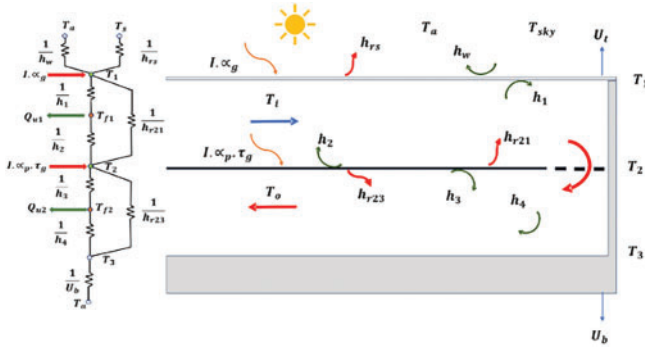


Fig. 5. Heat transfer coefficients and thermal resistance network.

For the absorber plate at T_2 , the heat balance equation is given as:

$$I \alpha_p \tau_g = h_2 (T_2 - T_{f1}) + h_3 (T_2 - T_{f2}) + h_{r21} (T_2 - T_1) + h_{r23} (T_2 - T_3). \quad (3)$$

For the air in the second channel at T_{f2} , the heat balance equation is given as:

$$h_3 (T_2 - T_{f2}) = h_4 (T_{f2} - T_3) + Q_{u2}. \quad (4)$$

For the insulation layer at T_3 , the heat balance equation is expressed as:

$$h_4 (T_{f2} - T_3) + h_{r23} (T_2 - T_3) = U_b (T_3 - T_a). \quad (5)$$

The terms Q_{u1} and Q_{u2} represent the useful energy obtained from the first and second passes, respectively. After simplification and integration, these variables are expressed in their final forms as follows:

$$Q_{u1} = 2 \dot{m} c_p (T_{f1} - T_{f1i}) / WL, \quad (6)$$

$$Q_{u2} = 2 \dot{m} c_p (T_{f2} - T_{f2i}) / WL, \quad (7)$$

$$T_{f1} = (T_{f1o} + T_{f1i}) / 2 \quad (8)$$

$$T_{f2} = (T_{f2o} + T_{f2i}) / 2. \quad (9)$$

By applying the necessary simplifications and substitutions for the (6) to (9), where $\lambda_1 = \frac{2 \dot{m} c_p}{W_1 L_1}$, $\lambda_2 = \frac{2 \dot{m} c_p}{W_2 L_2}$, $S_1 = I \alpha_g$, and $S_2 = I \alpha_p \tau_g$ a set of five heat transfer equations is developed.

$$(h_1 + h_{r21} + U_t) T_1 - h_1 T_{f1} - h_{r21} T_2 = S_1 + U_t T_a, \quad (10)$$

$$h_1 T_1 - (h_1 + h_2 + \lambda_1) T_{f1} + h_2 T_2 = -\lambda_1 T_{f1i}, \quad (11)$$

$$\begin{aligned} & -h_{r21} T_1 - h_2 T_{f1} + (h_2 + h_3 + h_{r21} + h_{r23}) T_2 \\ & - h_3 T_{f2} - h_{r23} T_3 = S_2 \end{aligned} \quad (12)$$

$$2 \lambda_2 T_{f1} + h_3 T_2 - (h_3 + h_4 + \lambda_2) T_{f2} + h_4 T_3 = \lambda_2 T_{f1i} \quad (13)$$

$$-h_{r23} T_2 - h_4 T_{f2} + (h_{r23} + U_b + h_4) T_3 = U_b T_a \quad (14)$$

The above equations for the DPSAC can be stated in the subsequent 5×5 matrix form, where $[A]$ is the matrix of coefficients, and $[T]$ represents the vector of unknown temperatures: T_1 , T_{f1} , T_2 , T_{f2} , and T_3 . The mean temperature vector is found using matrix inversion, $[T] = [A]^{-1} [B]$.

Ong [16] detailed the method for determining the radiative heat transfer coefficients, specifically h_{r1-s} , h_{r21} , and h_{r23} , which are calculated as follow:

From the transparent cover to the sky h_{rg-s} :

$$h_{r1-s} = \frac{\sigma \epsilon_1 (T_1 + T_s) (T_1^2 + T_s^2) (T_1 - T_s)}{(T_1 - T_a)}. \quad (15)$$

For the absorber to the transparent cover h_{rp-g} :

$$h_{r21} = \frac{\sigma (T_1^2 + T_2^2) (T_1 + T_2)}{\left(\frac{1}{\epsilon_1} + \frac{1}{\epsilon_1} - 1 \right)}. \quad (16)$$

Form the absorber to the insulation layer h_{rp-b} :

$$h_{r23} = \frac{\sigma (T_2^2 + T_3^2) (T_2 + T_3)}{\left(\frac{1}{\epsilon_2} + \frac{1}{\epsilon_3} - 1 \right)}. \quad (17)$$

Here, σ represents the Stefan-Boltzmann constant, while ϵ_1 , ϵ_2 , and ϵ_3 denote the emissivity of the glazing, the absorbing surface, and the insulation layer, respectively.

The sky temperature (T_s), which is related to the ambient temperature (T_a), (18). The convective heat transfer coefficient caused by wind (h_w), which depends on wind speed (V_w), is estimated by (19). The overall top heat loss coefficient (U_t) is the sum of h_w and h_{r1-s} , as described in (20). Additionally, conductive heat loss through the back layer (U_b) is incorporated into the analysis and is calculated using (21) [14], [16].

$$T_s = 0.0552 T_a^{1.5}. \quad (18)$$

$$h_w = 2.8 + 3.3 V_w. \quad (19)$$

$$U_t = h_w + h_{r1-s}. \quad (20)$$

$$U_b = \frac{1}{i = \sum_1^n (x_{bi}/k_{bi}) + 1/h_w} \quad (21)$$

The following equation is used to determine the convective heat coefficients within the flow passes [14], [16]:

$$h_1 = h_2 = h_3 = h_4 = Nu \frac{k}{D_h}. \quad (22)$$

The Nusselt number (Nu) relates to the thermal conductivity of air (k) and the hydraulic diameter of the ducts (D_h). Depending on the flow regime, specific formulations are applied: laminar flow occurs when the Reynolds number (Re) is less than 2300, transitional flow corresponds to $2300 < Re < 6000$, and turbulent flow applies when Re exceeds 6000. The calculation methods for both Nu and Re are derived from the approaches detailed in references [16], [17].

The following correlation is used to calculate the Re for flow passing within the air channel:

$$Re = \frac{\dot{m} D_h}{A_{ch} \mu} \quad (23)$$

D_h estimated as following:

$$D_h = \frac{4WB}{2(W+B)}. \quad (24)$$

For the laminar flow where $Re < 2300$:

$$Nu = 5.4 + \frac{0.00190 \left[Re Pr \left(\frac{D_h}{L} \right) \right]^{1.71}}{1 + 0.00563 \left[Re Pr \left(\frac{D_h}{L} \right) \right]^{1.71}}. \quad (25)$$

For the transition flow where $2300 < Re < 6000$:

$$Nu = 0.116 \left(Re^{\frac{2}{3}} - 125 \right) Pr^{\frac{1}{3}} + \left[1 + \left(\frac{D_h}{L} \right)^{\frac{2}{3}} \right] \left(\frac{\mu}{\mu_w} \right)^{0.14} \quad (26)$$

For turbulence flow where $Re > 6000$

$$Nu = 0.0158 Re^{0.8}. \quad (27)$$

The thermophysical properties of air are estimated using the following equations, which account for the mean air temperature along the collector [16].

Specific Heat (C_p):

$$C_p = 1.0057 + 0.000066 (T - 27) \quad (28)$$

Density (ρ):

$$\rho = 1.1774 - 0.00359 (T - 27) \quad (29)$$

Thermal conductivity (k):

$$k = 0.02624 + 0.0000758 (T - 27) \quad (30)$$

Viscosity (μ):

$$\mu = [1.983 + 0.00184 (T - 27)] \times 10^{-5} \quad (31)$$

2.3. Data Reduction of the Experiments

The formula used to calculate the instantaneous efficiency of the SAC is provided in Machi et al. [18]:

$$\eta = \frac{Q_u}{A_p \times I} \quad (32)$$

where A_p represents the collector's projected area in square meters (m^2), I indicates the solar radiation incident on the collector in (W/m^2), and Q_u refers to the useful energy gained by the collector, calculated as:

$$Q_u = \dot{m} C_p \Delta T \quad (33)$$

where \dot{m} represents the MFR (kg/s), determined using (34), C_p is the specific heat capacity of air ($J/kg^\circ C$), and ΔT

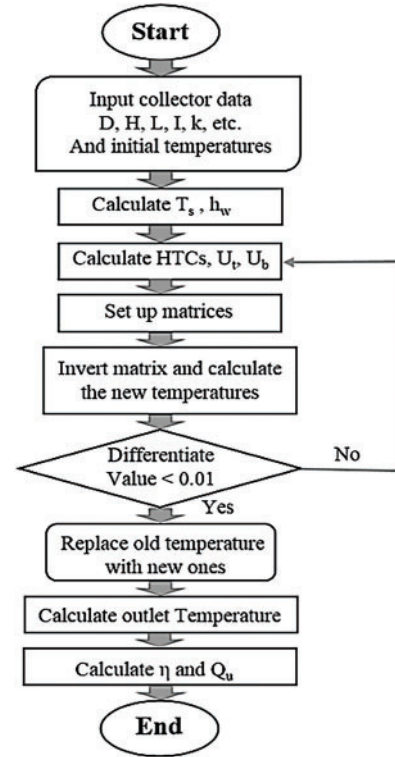


Fig. 6. Flowchart for theoretical procedure.

indicates the temperature difference of the air as it flows through the collector (28), (29).

$$\dot{m} = C_d \times A_o \times \left[\frac{2 \times \rho \times \Delta P_o}{1 - \beta^4} \right]^{1/2} \quad (34)$$

where C_d represents the discharge coefficient of the orifice plate, A_o is the area of the orifice plate, and ρ represents the air density measured at the exit temperature. Additionally, ΔP_o is the pressure drop through the orifice plate, and β the ratio of the orifice diameter to the duct diameter.

The MATLAB-based program, outlined in Fig. 6, starts with initial guesses for air stream, plastic cover, absorber, and insulation temperatures, along with input parameters. It calculates sky temperature, wind convection coefficients, and heat transfer characteristics. Matrices $[A]$, $[T]$, and $[B]$ are used to update temperatures iteratively until differences are below $0.01^\circ C$, typically within six iterations. Finally, the program outputs the outlet temperatures, useful energy gain, and efficiency. The relevant parameters are detailed in Table II.

3. RESULT AND DISCUSSIONS

This study focuses on analysing the factors affecting the performance of SACs using mathematical modelling. The model was validated with experimental data collected over several days between August and September 2023. The experimental work involved two MFRs: 0.0103 kg/s and 0.01317 kg/s .

Fig. 7. shows solar radiation and ambient temperature (T_a) trends for MFR of 0.01317 kg/s and 0.0103 kg/s . Solar radiation peaks at 934.28 W/m^2 and 933.2 W/m^2 for the

TABLE II: PARAMETER USED IN THE SIMULATION

Parameter	Value
Absorptivity of plastic cover	$\alpha_g = 0.1$
Absorptivity of absorber	$\alpha_p = 0.9$
Emissivity of the plastic	$\epsilon_g = 0.8$
Emissivity of the black absorber	$\epsilon_p = 0.9$
Emissivity of the insulation	$\epsilon_b = 0.9$
Transmissivity of plastic cover	$\tau_g = 0.9$
Density of air	Equation (29)
Viscosity of air	Equation (31)
Thermal conductivity of air	Equation (30)
Specific heat of air	Equation (28)

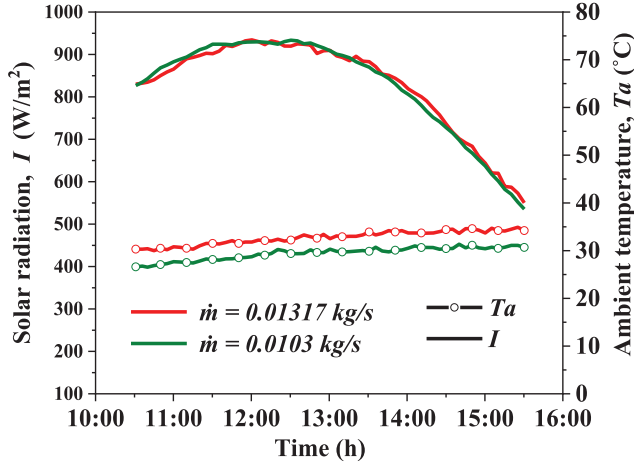


Fig. 7. Ambient temperature and solar radiation variations over time.

respective MFRs, while T_a reaches 34.9°C and 31.3°C. Both parameters follow a day pattern, increasing in the morning, peaking at midday, and declining in the afternoon. These trends provide essential context for evaluating the thermal performance of the SAC.

Figs. 8 and 9 compare the simulated and experimental results for both the outlet temperature and thermal efficiency, respectively. The model shows strong agreement with experimental data, with R^2 values of 0.989 for outlet temperature and 0.917 for thermal efficiency. This indicates that the model explains 98.9% of the variation in outlet temperature and 91.7% in thermal efficiency, demonstrating its accuracy in predicting DPSAC performance. Validation was conducted using experimental data at an MFR of 0.0103 kg/s, further confirming the reliability of the model under the tested conditions.

Subsequently, the validated model was applied to additional experimental data collected at MFRs of 0.0088, and 0.01317 kg/s. For these cases, the R^2 values for the simulated outlet temperature ranged from 0.932 to 0.989, indicating a strong correlation and confirming that the model effectively explains the majority of the variance in the experimental data.

For thermal efficiency, the R^2 values for the comparison between experimental and simulated data ranged from 0.808 to 0.917, indicating a moderate to strong correlation. This range reflects the model's capability to account for a substantial portion of the variance in thermal efficiency across different test conditions.

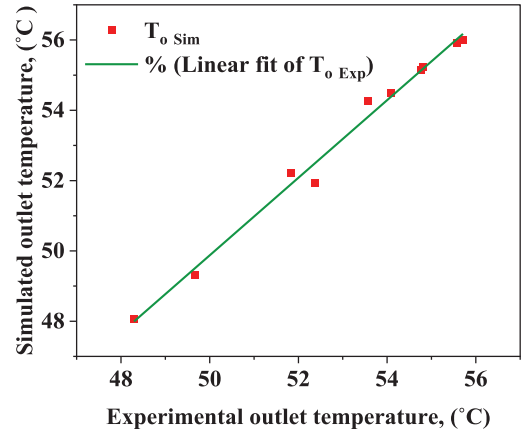


Fig. 8. Validation of simulated data with experimental data for outlet temperature.

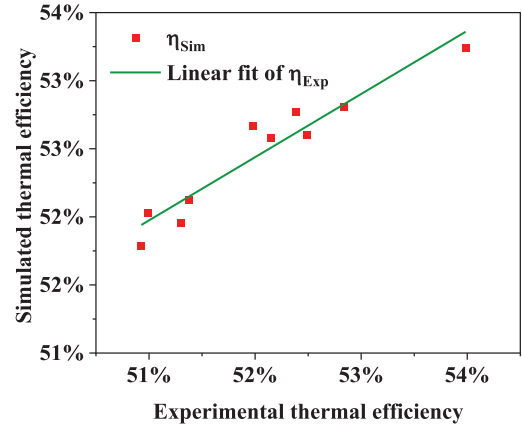


Fig. 9. Validation of simulated data with experimental measurements for thermal efficiency.

Figs. 10 and 11 compare the simulated outlet temperature ($T_{o\text{Sim}}$) and experimental outlet temperature ($T_{o\text{Exp}}$) for the tested MFRs along with the ambient temperature. At 0.0103 kg/s, the highest experimental temperature recorded was 52.7°C, while the maximum simulated temperature was 53.2°C. At 0.01317 kg/s, the highest experimental temperature recorded was 54°C, while the maximum simulated temperature was 54.6°C. For both cases, the $T_{o\text{Sim}}$ and $T_{o\text{Exp}}$ curves show excellent agreement, demonstrating the model's accuracy in predicting the system's thermal behaviour. Both outlet temperature curves follow the typical daily trend, peaking at midday and decreasing as solar radiation declines, while the ambient temperature remains relatively stable. The strong correlation in both figures confirms the model's reliability for performance prediction under varying conditions.

Figs. 12 and 13 compare the simulated useful energy output (Qu_{Sim}) and experimental useful energy output (Qu_{Exp}) for the tested MFRs, along with the incident energy (Qi).

In both figures, Qu_{Sim} and Qu_{Exp} closely follow the trend of the incident energy (Qi), with outputs increasing in the morning, peaking at midday, and decreasing in the afternoon as solar radiation declines. This alignment confirms the model's reliability in predicting system performance. The maximum useful energy output for an MFR of 0.0103 kg/s was 258.6 W experimentally, while the simulated value reached 263.5 W. For 0.01317 kg/s, the experimental maximum output was 285.1 W, compared to

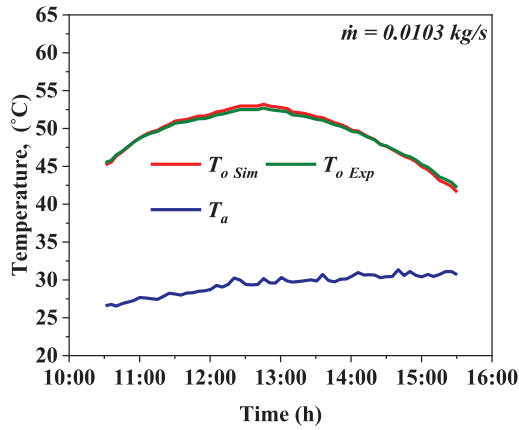


Fig. 10. Simulated and experimental outlet temperatures at 0.0103 kg/s.

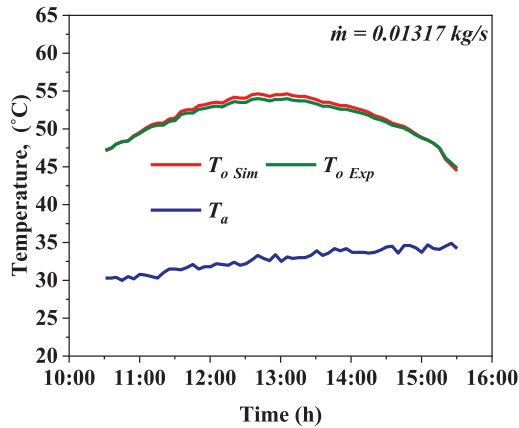


Fig. 11. Simulated and experimental outlet temperatures at 0.01317 kg/s.

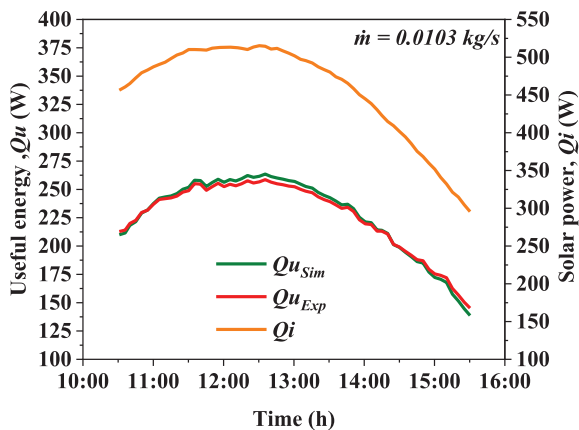


Fig. 12. Simulated and experimental useful energy at 0.0103 kg/s.

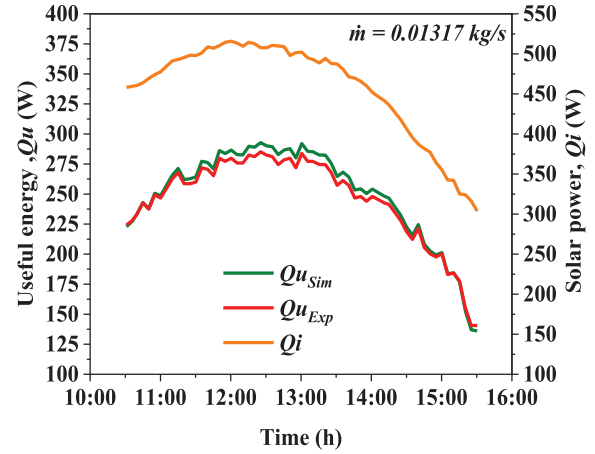


Fig. 13. Simulated and experimental useful energy at 0.01317 kg/s.

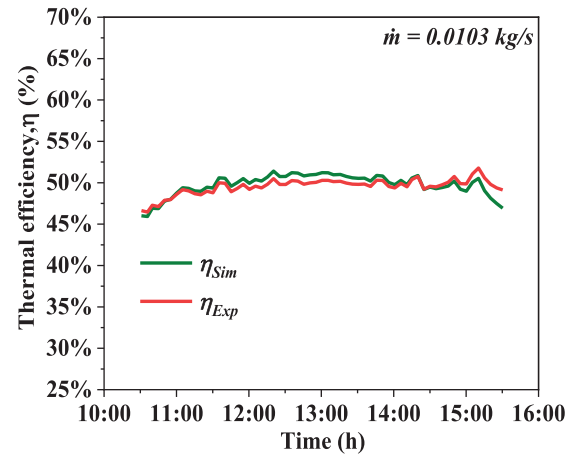


Fig. 14. Simulated and experimental instantaneous thermal efficiency at 0.0103 kg/s.

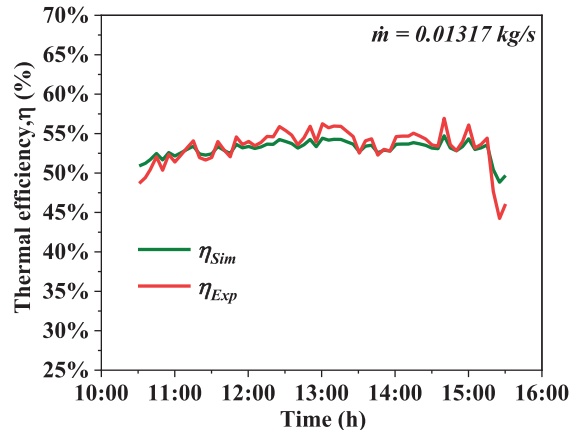


Fig. 15. Simulated and experimental instantaneous thermal efficiency at 0.01317 kg/s.

a simulated value of 292.7 W. These results demonstrate excellent agreement and highlight the model's accuracy.

Figs. 14 and 15 present the comparison between the simulated (η_{Sim}) and experimental (η_{Exp}) instantaneous thermal efficiency for the tested MFRs. Both figures demonstrate a strong correlation, with the simulated and experimental curves closely following similar trends throughout the test period. These results validate the model's high accuracy in predicting instantaneous thermal efficiency across different flow rates, despite minor variations caused by dynamic solar radiation. For a MFR of 0.0103 kg/s the maximum experimental efficiency was

51.7%, while the simulated value reached 52.3% as seen in Fig. 14. Similarly, for 0.01317 kg/s the maximum experimental efficiency was 56.9%, compared to a simulated efficiency of 54.7% (Fig. 15).

Fig. 16 demonstrates the change of outlet temperature with MFRs under different solar radiation intensities. The figure demonstrates that higher solar radiation leads to an increase in outlet temperature as the collector absorbs more thermal energy. However, as the MFR increases, the outlet temperature decreases because the air spends

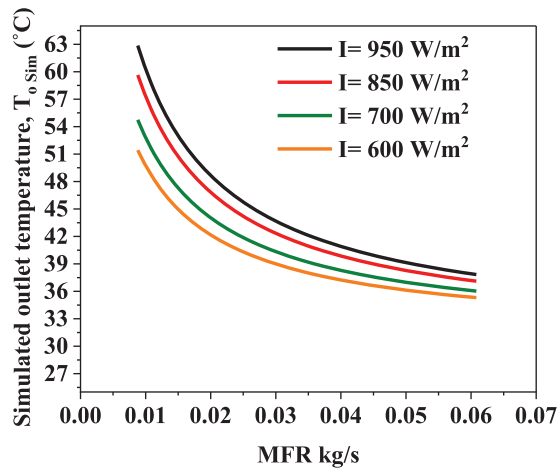


Fig. 16. Simulated outlet temperature vs. MFR at different solar intensity.

less time in contact with the absorber plate, reducing heat transfer.

At sufficiently high MFRs, the outlet temperature approaches the inlet temperature, diminishing the collector's ability to provide a meaningful temperature difference, which is critical for many applications.

Further increases in airflow rates also lead to unnecessary pumping power requirements, resulting in higher energy consumption and operational costs. This situation is particularly disadvantageous from an exergetic perspective, as it lowers the overall efficiency and economic feasibility of the system. The figure also highlights that the influence of solar intensity is more pronounced at lower MFRs, where the air has more time to absorb the additional energy provided by higher solar radiation. As the MFR increases, the curves for different solar intensities begin to converge, indicating that the impact of solar radiation becomes less significant at high flow rates. These findings emphasize the importance of optimizing MFRs to balance thermal performance and energy consumption effectively, particularly under varying solar radiation conditions.

Fig. 17 represented the difference of thermal efficiency with MFR. As MFR increases, thermal efficiency improves initially due to enhanced convective heat transfer, which facilitates better energy transfer from the absorber plate to the air. However, beyond a certain point, further increases in MFR reduce efficiency due to a diminished temperature difference between the inlet and outlet air, particularly with the simulated fixed inlet temperature of 31.1 °C.

The effect of solar radiation becomes especially pronounced at higher flow rates. At higher MFRs, the convective heat transfer from the absorber plate to the air becomes more significant, increasing the system's dependence on adequate solar radiation to sustain its thermal performance. When the available solar radiation is insufficient to offset the heat dissipation from the absorber plate, the collector's efficiency decreases, highlighting the importance of matching solar intensity with the operational MFR.

The preferred operating range for the proposed collector was found to be between 0.01 kg/s and 0.025 kg/s.

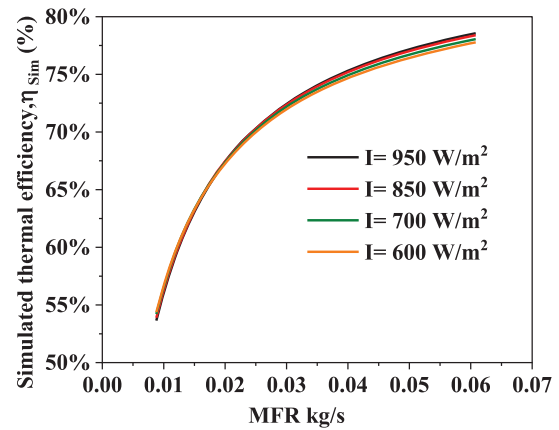


Fig. 17. Simulated thermal efficiency vs. MFR at different solar intensity.

Within this range, the collector maintains an acceptable temperature difference between the inlet and outlet air, ensuring efficient performance across various solar intensities. These findings underscore the need for careful optimization of the MFR to balance thermal efficiency and outlet temperature while accounting for solar radiation variability.

4. CONCLUSION

A mathematical model was developed to evaluate the performance of double-pass solar air collectors (DPSACs) under various airflow rates, validated using experimental data. The thermal efficiency, outlet temperature, and useful energy output were analyzed, leading to the following significant conclusions:

- The model demonstrated strong agreement with experimental results, with R^2 values of 0.989 for outlet temperature and 0.917 for thermal efficiency, highlighting its reliability in predicting DPSAC performance under several MFRs and solar radiation levels.
- The thermal efficiency of the DPSAC increases as the MFR rises initially, due to improved convective heat transfer. However, at higher flow rates, the efficiency gains diminish because the air spends less time in the collector, reducing the overall heat absorbed and limiting the collector's ability to achieve significant temperature differences.
- The preferred operating range for the proposed DPSAC was identified as 0.01 kg/s to 0.025 kg/s, balancing thermal efficiency and outlet temperature. At this range, the system demonstrates reliable performance across different solar intensities.
- Solar radiation intensity significantly impacts performance at lower MFRs, where the air remains in the collector longer, allowing for greater heat absorption. Conversely, at higher MFRs, the influence of solar radiation becomes less pronounced due to reduced air residence time.
- The findings underscore the importance of optimizing MFRs and operational parameters for different

applications, ensuring both energy efficiency and economic viability.

- Finally, the validated model serves as a reliable tool for predicting the performance of DPSACs and can guide the design and optimization of future systems for drying and thermal energy applications.

ACKNOWLEDGMENT

This work was supported by the Stipendium Hungaricum Program and the Doctoral School of Mechanical Engineering, Institute of Technology, the Hungarian University of Agriculture and Life Sciences, Gödöllő, Hungary.

CONFLICT OF INTEREST

Authors declare that we do not have any conflict of interest.

REFERENCES

- [1] Habtay G, Al-neama MA, Buzas J, Farkas I. Experimental performance of solar air heaters for drying applications. *Eur J Energy Res.* 2021;1:4–10. doi: 10.24018/ejenergy.2021.1.5.29.
- [2] Zhu Q, Farkas I, Buzas J. Influencing factors used for performance evaluation of solar dryers. *Eur J Energy Res.* 2024;4:8–14. doi: 10.24018/ejenergy.2024.4.3.145.
- [3] Machi MH, Al-Neama MA, Buzás J, Farkas I. Energy-based performance analysis of a double pass solar air collector integrated to triangular shaped fins. *Int J Energy Environ Eng.* 2022;13:219–29. doi: 10.1007/s40095-021-00422-z.
- [4] Goel V, Hans VS, Singh S, Kumar R, Pathak SK, Singla M, et al. A comprehensive study on the progressive development and applications of solar air heaters. *Sol Energy.* 2021;229:112–47. doi: 10.1016/j.solener.2021.07.040.
- [5] Hegde AK, Pai R, Karanth KV. Performance augmentation of solar air heaters: a comprehensive analysis. *Sol Energy.* 2023;253:527–53. doi: 10.1016/j.solener.2023.01.031.
- [6] Omotosho E, Hackney P. Performance prediction of single-pass and multi-pass low-cost solar air heater. *Therm Sci Eng Prog.* 2024;47:102322. doi: 10.1016/j.tsep.2023.102322.
- [7] Karim MA, Perez E, Amin ZM. Mathematical modelling of counter flow v-grove solar air collector. *Renew Energy.* 2014;67:192–201. doi: 10.1016/j.renene.2013.11.027.
- [8] Singh VP, Jain S, Karn A, Kumar A, Dwivedi G, Meena CS, et al. Mathematical modeling of efficiency evaluation of double-pass parallel flow solar air heater. *Sustain.* 2022;14:1–22. doi: 10.3390/su141710535.
- [9] Sun C, Liu Y, Duan C, Zheng Y, Chang H, Shu S. A mathematical model to investigate on the thermal performance of a flat plate solar air collector and its experimental verification. *Energy Convers Manag.* 2016;115:43–51. doi: 10.1016/j.enconman.2016.02.048.
- [10] Bangura ABM, Hantoro R, Fudholi A, Uwitije PD. Mathematical model of the thermal performance of double-pass solar collector for solar energy application in sierra leone. *Int J Renew Energy Dev.* 2022;11:347–55. doi: 10.14710/IJRED.2022.41349.
- [11] El-Sebaï AA, Al-Snani H. Effect of selective coating on thermal performance of flat plate solar air heaters. *Energy.* 2010;35:1820–8. doi: 10.1016/j.energy.2009.12.037.
- [12] Lin W, Ren H, Ma Z. Mathematical modelling and experimental investigation of solar air collectors with corrugated absorbers. *Renew Energy.* 2020;145:164–79. doi: 10.1016/j.renene.2019.05.129.
- [13] Saravanakumar PT, Somasundaram D, Matheswaran MM. Thermal and thermo-hydraulic analysis of arc shaped rib roughened solar air heater integrated with fins and baffles. *Sol Energy.* 2019;180:360–71. doi: 10.1016/j.solener.2019.01.036.
- [14] Assadeg J, Al-Waeli AHA, Fudholi A, Sopian K. Energetic and exergetic analysis of a new double pass solar air collector with fins and phase change material. *Sol Energy.* 2021;226:260–71. doi: 10.1016/j.solener.2021.08.056.
- [15] Fudholi A, Sopian K, Ruslan MH, Othman MY, Yahya M. Thermal efficiency of double pass solar collector with longitudinal fins absorbers. *Am J Appl Sci.* 2011;8:254–60. doi: 10.3844/ajassp.2011.254.260.
- [16] Ong KS. Thermal performance of solar air heaters: mathematical model and solution procedure. *Sol Energy.* 1995;55:93–109. doi: 10.1016/0038-092X(95)00021-I.
- [17] Naphon P. On the performance and entropy generation of the double-pass solar air heater with longitudinal fins. *Renew Energy.* 2005;30:1345–57. doi: 10.1016/j.renene.2004.10.014.
- [18] Machi MH, Farkas I, Buzas J. Enhancing thermal efficiency of double-pass solar air collectors: a comparative study on the role of V-angled perforated fins. *Energy Rep.* 2024;12:481–94. doi: 10.1016/j.egyr.2024.06.048.